J. Fluid Mech. (1986), *vol.* 162, 1–22
Printed in Great Britain

Spectral solutions for three-dimensional triple-deck flow over surface topography

By P. W. DUCK
Department of Mathematics, University of Manchester, Manchester M13 9PL

AND O. R. BURGGRAF
Department of Aeronautical and Astronautical Engineering, The Ohio State University, Columbus, Ohio 43210

(Received 24 November 1984 and in revised form 4 June 1985)

The effect of surface topography on an otherwise two-dimensional boundary-layer flow is investigated. The flow is assumed to be steady, laminar and incompressible, and is described by triple-deck theory. The basic problem reduces to the solution of a form of the nonlinear three-dimensional boundary-layer equations, together with an interaction condition. The solutions are obtained by a spectral method, with the computations carried out iteratively in Fourier-transform space. Numerical results are presented for several cases including three-dimensional separation. Comparison is made with the predictions of linearized theory. The decay corridor observed by Smith is confirmed for one localized configuration, but not for another having a broader height distribution.

1. Introduction

Triple-deck theory was developed independently by Messiter (1970), Neiland (1969) and Stewartson & Williams (1969) to describe situations in which flow disturbances become large enough that classical boundary-layer theory fails. Examples of such flows are boundary-layer separation (Stewartson & Williams 1969; Rizzetta, Burggraf & Jenson 1978) and the flow near a trailing edge (Stewartson 1969; Jobe & Burggraf 1974). In both cases the singularity arising in boundary-layer theory is eliminated by the inclusion of a viscous–inviscid interaction condition in the triple deck. (For a recent review see Stewartson (1981).)

The original theory was developed for two-dimensional flows, but recently has been extended to three dimensions. Burggraf (1976) reported on the linearized theory for supersonic flow past a 'split-ramp' configuration for which the ramp angle varied (discontinuously) in the cross-flow direction. Smith (1976) studied the effect of a three-dimensional constriction inside a pipe, while Smith, Sykes & Brighton (1977) considered the effect of a small three-dimensional surface perturbation on a two-dimensional oncoming boundary layer. Sykes (1978) has since extended this analysis to include the effect of stable stratification, while Duck (1980) included the effects of an unsteady perturbation on the flow.

However, in most of these three-dimensional studies only linearized solutions were obtained, valid for vanishingly small perturbations. (An alternative limiting case is the study by Duck (1980), who obtained linearized solutions by considering the limit of increasing rapid variations of surface irregularity.) The full nonlinear problem requires a numerical solution of the boundary-layer equations. A number of corres-

ponding nonlinear two-dimensional problems have been treated successfully, and are now fairly well understood (see, e.g., Rizzetta *et al.* 1978; Sykes 1978). Smith (1980) considered the three-dimensional 'free-interaction' problem relevant to pipe flows, while Sykes (1980) obtained solutions of Smith's equations relevant to flows over surface irregularities inside pipes. Sykes also interpreted his study as that of an external flow with infinitely stable stratification. The corresponding three-dimensional interacting-flow problem has not been treated as yet. Sykes (1980) noted that such problems proved intractable using his finite-difference method, because of the exponential growth of eigensolutions. Consequently, to obtain convergent solutions, he was forced to cut off all but a few wavenumber modes in the crossflow direction. One aim of this paper is to present a satisfactory method of obtaining solutions for three-dimensional incompressible flows of this type.

The standard approach to solving the linearized equations in two- and three-dimensional triple-deck situations has been to use Fourier-transform methods, and this was the genesis of a spectral method developed by Burggraf & Duck (1981) for solving the full nonlinear two-dimensional triple-deck problem. In this previous paper results of spectral computations were shown to compare very favourably with standard numerical (i.e. finite-difference) techniques. In the present paper we extend this two-dimensional procedure to external three-dimensional situations, for which finite-difference methods have not proven successful.

2. Equations of motion

The flow structure is given in some detail by Smith *et al.* (1977), and so details here will be kept to a minimum. The basic flow configuration is shown in figure 1. We consider the flow past a flat plate, on which is situated a small protuberance. If U_∞ is the flow speed far from the plate, L the distance of the protuberance from the leading edge of the plate and ν the kinematic viscosity of the fluid, a Reynolds number may be defined by

$$Re = U_\infty L/\nu, \tag{2.1}$$

which we shall assume large. As in previous triple-deck analyses, it is convenient to define a small parameter

$$\epsilon = Re^{-\frac{1}{8}}. \tag{2.2}$$

We assume also that the flow is everywhere steady, laminar and incompressible. Cartesian coordinates (Lx, Ly, Lz) are chosen with origin near the surface irregularity, while the flow velocity is $(U_\infty u, U_\infty v, U_\infty w)$ and the pressure is written as $\rho U_\infty^2 p$, where ρ is the density of the fluid. Far from the plate the flow is directed along the positive x-axis. Thus we restrict the unperturbed oncoming boundary layer to two-dimensional type, for which there is no crossflow component of velocity.

We consider surface irregularities of height $O(L\epsilon^5)$ and length and width $O(L\epsilon^3)$. The horizontal coordinates are then rescaled as

$$\left.\begin{aligned} X &= \frac{x}{\epsilon^3} = O(1), \\ Z &= \frac{z}{\epsilon^3} = O(1) \end{aligned}\right\} \tag{2.3}$$

The 'main deck' is defined by the vertical scaling

$$\tilde{y} = \frac{y}{\epsilon^4} = O(1). \tag{2.4}$$

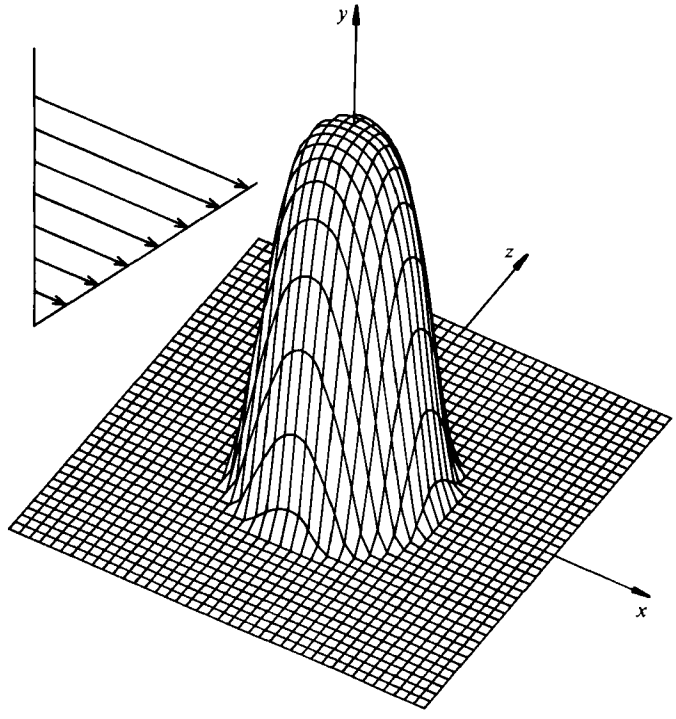

FIGURE 1. Schematic of lower-deck flow past cosine-squared hump.

Smith *et al.* (1977) found the solution to develop as

$$\left.\begin{aligned} u &= U_{\mathrm{B}}(\tilde{y}) + \epsilon A(X,Z)\, U'_{\mathrm{B}}(\tilde{y}) + O(\epsilon^2), \\ w &= \frac{\epsilon^2 D(X,Z)}{U_{\mathrm{B}}(\tilde{y})} + O(\epsilon^3), \\ v &= -\epsilon^3 \frac{\partial A}{\partial X}\, U_{\mathrm{B}}(\tilde{y}), \\ p &= \epsilon^2 P(X,Z), \end{aligned}\right\} \tag{2.5}$$

where

$$\frac{\partial D}{\partial X} = -\frac{\partial P}{\partial Z},$$

and $U_{\mathrm{B}}(\tilde{y})$ is the oncoming velocity profile (for example the Blasius profile).

The pressure is governed by Laplace's equation in the 'upper deck' where

$$y = O(\epsilon^3). \tag{2.6}$$

Matching with the main-deck solution yields a relationship between $P(X,Z)$ and $A(X,Z)$, namely

$$P(X,Z) = -\frac{1}{2\pi} \int_{-\infty}^{\infty} \int_{-\infty}^{\infty} \frac{\partial^2 A/\partial \xi^2 \, \mathrm{d}\xi \, \mathrm{d}\zeta}{\{(X-\xi)^2 + (Z-\zeta)^2\}^{\frac{1}{2}}}. \tag{2.7}$$

Since the main deck fails to satisfy the surface boundary conditions a 'lower deck' is required, where the motion is of a viscous nature. Here

$$(u, v, w, p, y) = (\epsilon U, \epsilon^3 \tilde{V}, \epsilon W, \epsilon^2 P, \epsilon^5 \tilde{Y}), \tag{2.8}$$

and the equations of motion, to leading order, are

$$\frac{\partial U}{\partial X}+\frac{\partial \tilde{V}}{\partial \tilde{Y}}+\frac{\partial W}{\partial Z}=0, \tag{2.9a}$$

$$U\frac{\partial U}{\partial X}+\tilde{V}\frac{\partial U}{\partial \tilde{Y}}+W\frac{\partial U}{\partial Z}=-\frac{\partial P}{\partial X}+\frac{\partial^2 U}{\partial \tilde{Y}^2}, \tag{2.9b}$$

$$U\frac{\partial W}{\partial X}+\tilde{V}\frac{\partial W}{\partial \tilde{Y}}+W\frac{\partial W}{\partial Z}=-\frac{\partial P}{\partial Z}+\frac{\partial^2 W}{\partial \tilde{Y}^2}. \tag{2.9c}$$

The boundary conditions are

$$\begin{aligned} &U=\tilde{V}=W=0 \quad \text{on} \quad \tilde{Y}=hF(X,Z),\\ &U\sim U'_{\mathrm{B}}(0)\,[\tilde{Y}+A(X,Z)]\\ &W\sim \frac{D(X,Z)}{U'_{\mathrm{B}}(0)\,\tilde{Y}} \quad \text{as } \tilde{Y}\to\infty,\\ &U\sim U'_{\mathrm{B}}(0)\,\tilde{Y}, \quad V,W,P\to 0 \quad \text{as } X\to-\infty, \end{aligned} \tag{2.10}$$

where the prime denotes differentiation with respect to a single argument.

It is convenient to make the following transformations:

$$\begin{aligned} Y&=\tilde{Y}-hF(X,Z),\\ V&=\tilde{V}-UhF_X-WhF_Z, \end{aligned} \tag{2.11}$$

and also we may take $U'_{\mathrm{B}}(0)=1$ without loss of generality, as shown by Smith *et al.* (1977). Equation (2.9) remains unchanged, with Y and V replacing $\tilde{Y}$ and $\tilde{V}$ respectively, while

$$U=V=W=0 \quad \text{on } Y=0, \tag{2.12a}$$

$$U\sim Y+A(X,Z)+hF(X,Z) \quad \text{as } Y\to\infty \tag{2.12b}$$

(the remaining boundary conditions are unchanged). We now have a closed mathematical problem. Smith *et al.* (1977) considered the limit $h\to 0$, and then obtained a linearized solution about a uniform shear flow. In §3 we consider a solution of the full nonlinear problem, for $h=O(1)$.

3. Method of solution

We now extend the two-dimensional work of Burggraf & Duck (1981) to three dimensions. As before, the analysis is restricted to the lower deck, which can be matched to the outer flow by use of analytical results for the linear equations of the main and upper decks. First split the X-component of velocity into its perturbed and unperturbed parts:

$$U=\hat{U}+Y. \tag{3.1}$$

After differentiating (2.9b) with respect to Y, (2.9a–c) become

$$\hat{U}_X+V_Y+W_Z=0, \tag{3.2a}$$

$$Y\hat{U}_{XY}-W_Z-\hat{U}_{YYY}=\hat{U}_Y W_Z-V\hat{U}_{YY}-\hat{U}\hat{U}_{XY}-W_Y\hat{U}_Z-W\hat{U}_{ZY}, \tag{3.2b}$$

$$YW_X-W_{YY}+P_Z=-\hat{U}W_X-VW_Y-WW_Z. \tag{3.2c}$$

Note that Smith *et al.* (1977) concerned themselves with the system (3.2) with the right-hand-side terms neglected.

We find it convenient to introduce the perturbation streamwise shear $\hat{\tau}$ defined by

$$\hat{\tau} = \frac{\partial \hat{U}}{\partial Y}. \tag{3.3}$$

The double Fourier transform is denoted by a double asterisk; thus, for example,

$$\tau^{**}(k, l, Y) = \int_{-\infty}^{\infty} \int_{-\infty}^{\infty} \hat{\tau}(X, Y, Z)\, \mathrm{e}^{-\mathrm{i}kX - \mathrm{i}lZ}\, \mathrm{d}X\, \mathrm{d}Z. \tag{3.4}$$

Further, we also make a transformation in the Y-direction (for later use) by

$$Y = f(\eta),$$

where we shall assume

$$\left.\begin{aligned} 0 \leqslant \eta \leqslant \eta_\infty < 1, \\ 0 \leqslant Y \leqslant Y_\infty < \infty. \end{aligned}\right\} \tag{3.5}$$

Specifically, we choose

$$f(\eta) = \frac{\eta}{1-\eta}, \tag{3.6}$$

which is appropriate, given the decay of W indicated by (2.10) for $Y \to \infty$. Then the equations of motion (3.2) become

$$\mathrm{i}k \int_0^\eta \tau^{**} f'(\eta)\, \mathrm{d}\eta + \frac{1}{f'(\eta)} \frac{\partial V^{**}}{\partial \eta} + \mathrm{i}l W^{**} = 0, \tag{3.7a}$$

$$\mathrm{i}kf(\eta)\, \tau^{**} - \mathrm{i}l W^{**} - \frac{\partial^2 \tau^{**}}{\partial \eta^2} \frac{1}{[f'(\eta)]^2} + \frac{\partial \tau^{**}}{\partial \eta} \frac{f''(\eta)}{[f'(\eta)]^3}$$
$$= \left\{ \tau W_Z - \frac{V}{f'(\eta)} \frac{\partial \tau}{\partial \eta} - \tau_X \int_0^\eta \tau f'(\eta)\, \mathrm{d}\eta - \frac{W_\eta}{f'(\eta)} \int_0^\eta \tau_Z f'(\eta)\, \mathrm{d}\eta - W\tau_Z \right\}^{**}, \tag{3.7b}$$

$$\mathrm{i}kf(\eta)\, W^{**} - \frac{\partial^2 W^{**}}{\partial \eta^2} \frac{1}{[f'(\eta)]^2} + \frac{\partial W^{**}}{\partial \eta} \frac{f''(\eta)}{[f'(\eta)]^3} + \mathrm{i}l P^{**}$$
$$= -\left\{ W_X \int_0^\eta \tau f'(\eta)\, \mathrm{d}\eta + \frac{VW_\eta}{f'(\eta)} + WW_Z \right\}^{**}. \tag{3.7c}$$

The boundary conditions for this system are then

$$\left.\begin{aligned} V^{**} = W^{**} = 0 \quad \text{on } \eta = 0, \\ \tau^{**} = W^{**} \to 0 \quad \text{as } \eta \to \eta_\infty. \end{aligned}\right\} \tag{3.8}$$

One further boundary condition is required, and this arises from the X-component of the governing equation (2.9b) evaluated on $\eta = 0$, to give

$$\frac{1}{f'(0)} \tau_\eta^{**}(k, l, 0) = \mathrm{i}kP^{**}(k, l). \tag{3.9}$$

An interaction condition is needed to close the system of equations, and this arises from the boundary condition (2.12b), together with the relationship (2.7) linking P to A. Equation (2.12b) requires

$$\int_0^{\eta_\infty} f'(\eta)\, \tau^{**}\, \mathrm{d}\eta = A^{**} + hF^{**}, \tag{3.10}$$

while the double Fourier transform of (2.7) is

$$P^{**} = \frac{k^2 A^{**}}{(k^2+l^2)^{\frac{1}{2}}}. \tag{3.11}$$

Combining (3.10) and (3.11) to eliminate A^{**} yields the final equation

$$\frac{k^2}{(k^2+l^2)^{\frac{1}{2}}} \int_0^{\eta_\infty} \tau^{**} f'(\eta)\, \mathrm{d}\eta = P^{**} + \frac{hk^2 F^{**}}{(k^2+l^2)^{\frac{1}{2}}}. \tag{3.12}$$

The solution procedure is as follows. We choose a value of η_∞ (typically 0.95), such that (3.5) is replaced by

$$\left.\begin{aligned} 0 \leqslant \eta \leqslant \eta_\infty, \\ 0 \leqslant Y \leqslant Y_\infty \gg 1. \end{aligned}\right\} \tag{3.13}$$

Then (3.8) is approximated by

$$\tau^{**}(k,l,\eta_\infty) = W^{**}(k,l,\eta_\infty) = 0. \tag{3.14}$$

The range of (k,l) is to be truncated to

$$\left.\begin{aligned} k_{\min} \leqslant k \leqslant k_{\max}, \\ l_{\min} \leqslant l \leqslant l_{\max}, \end{aligned}\right\} \tag{3.15}$$

where $|k_{\min}|$, $|k_{\max}|$, $|l_{\min}|$, $|l_{\max}|$ are all suitably large. We then consider J, K and L points in the η-, k- and l-directions respectively, and define

$$\Delta\eta = \frac{\eta_\infty}{J-1}, \quad \Delta k = \frac{k_{\max}-k_{\min}}{K-1}, \quad \Delta l = \frac{l_{\max}-l_{\min}}{L-1}. \tag{3.16}$$

We now discretize (3.7) in the η-direction, using second-order finite differences, as, for example,

$$\left.\begin{aligned} \tau^{**}_{\eta}(k,l,\eta) &= \frac{\tau^{**}(k,l,\eta+\Delta\eta) - \tau^{**}(k,l,\eta-\Delta\eta)}{2\Delta\eta}, \\ \tau^{**}_{\eta\eta}(k,l,\eta) &= \frac{\tau^{**}(k,l,\eta+\Delta\eta) - 2\tau^{**}(k,l,\eta) + \tau^{**}(k,l,\eta-\Delta\eta)}{(\Delta\eta)^2}. \end{aligned}\right\} \tag{3.17}$$

Equation (3.9) is approximated by second-order-accurate backward differences (merely to avoid the introduction of image points), to yield

$$\tau^{**}(k,l,0) = -\tfrac{2}{3}\Delta\eta\, \mathrm{i}k f'(0)\, P^{**}(k,l) - \tfrac{1}{3}\tau^{**}(k,l,2\Delta\eta) + \tfrac{4}{3}\tau^{**}(k,l,\Delta\eta), \tag{3.18}$$

The integral in (3.12) is approximated using the trapezoidal rule.

The result is a matrix equation of the following form for each value of (k,l) (for the entire range of η):

$$\begin{bmatrix} \times & \times & \times & \times & & & & & \times \\ \times & \times & \times & \times & & & & & 0 \\ \times & \times & \times & \times & \times & \times & & & \times \\ \times & \times & \times & \times & \times & \times & & & 0 \\ & & \times & \times & \times & \times & \times & \times & \times \\ & & \times & \times & \times & \times & \times & \times & 0 \\ & & & & \times & \times & \times & \times & \times \\ & & & & \times & \times & \times & \times & 0 \\ & & & & & & \vdots & & \vdots \\ & & & & & \times & \times & \times & \times \\ & & & & & \times & \times & \times & 0 \\ & & & & & & & \times & \times \\ & & & & & & & \times & 0 \\ \times & \times & \times & \times & \times & \times & \ldots & \times & \times \end{bmatrix} \begin{bmatrix} W^{**}(\Delta\eta) \\ \tau^{**}(\Delta\eta) \\ W^{**}(2\Delta\eta) \\ \tau^{**}(2\Delta\eta) \\ W^{**}(3\Delta\eta) \\ \tau^{**}(3\Delta\eta) \\ W^{**}(4\Delta\eta) \\ \tau^{**}(4\Delta\eta) \\ \vdots \\ W^{**}(\eta_\infty - 2\Delta\eta) \\ \tau^{**}(\eta_\infty - 2\Delta\eta) \\ W^{**}(\eta_\infty - \Delta\eta) \\ \tau^{**}(\eta_\infty - \Delta\eta) \\ P^{**} \end{bmatrix} = \boldsymbol{R} \tag{3.19}$$

where a cross denotes a non-zero entry. The full bottom row occurs because of the interaction condition (3.12), while the half-full right-hand column occurs because of the pressure in the Z-component of momentum (the pressure was eliminated from the X-component by differentiation). At this stage, the equation of continuity is not required. Equation (3.19) is of a form suitable for Gaussian elimination, although not strictly of a banded nature.

The procedure adopted was to initiate the solution by setting the right-hand side of (3.19) to zero; thus solving (3.19) at each (k, l)-station, the first iteration produces solutions of the linear problem treated by Smith *et al.* (1977). When the entire (k, l)-domain has been covered once, the right-hand side of (3.6) is evaluated. It is not until this stage that the equation of continuity (3.7a) is required to evaluate V^{**}. The actual evaluation of the right-hand sides of (3.7b, c) is accomplished using the fast-Fourier-transform technique of Cooley & Tukey (1965). The transformation is applied twice for each iteration, with the first application transforming the spectral variables back into physical variables. The product terms involved in (3.7b, c) are then simply multiplied together and the results are then transformed back into spectral variables, again using the fast Fourier transform method. The process outlined above is repeated, but with a non-zero right-hand side in (3.19), again sweeping through the entire range of k and l. This procedure is applied repeatedly, until convergence is obtained. The fast-Fourier-transform method was chosen because $O(JKL(\log_2 K + \log_2 L))$ operations are required compared with $O(JKL(L+K))$ operations in the case of straightforward quadrature–inversion methods.

The surface perturbations treated here are symmetrical about $Z = 0$; in this case a number of very useful symmetries of the solution exist. In particular

$$\left.\begin{aligned} \tau^{**}(k, -l, Y) &= \tau^{**}(k, l, Y), \\ P^{**}(k, -l) &= P^{**}(k, l), \\ W^{**}(k, -l, Y) &= -W^{**}(k, l, Y), \\ \tau^{**}(-k, l, Y) &= \text{complex-conjugate}\{\tau^{**}(k, l, Y)\}, \\ P^{**}(-k, l) &= \text{complex-conjugate}\{P^{**}(k, l)\} \\ W^{**}(-k, l, Y) &= \text{complex-conjugate}\{W^{**}(k, l, Y)\}. \end{aligned}\right\} \tag{3.20}$$

By implementing these symmetries in the computer program, large savings result in computer storage and time. In addition, we note that because of the expected decay of the solution as $|X^2 + Z^2| \to \infty$ it is possible to set

$$\tau^{**}(0, l, Y) = W^{**}(0, l, Y) = P^{**}(0, l) = 0. \tag{3.21}$$

Usually around 20 iterations were required for convergence to about four-decimal-place accuracy. For large surface heights, a certain amount of under-relaxation was required; the pressure, for example, was updated from one iteration to the next according to the rule

$$P^{**}(k, l)^{\text{new}} = \omega P^{**\text{computed}}(k, l) + (1 - \omega) P^{**\text{old}}(k, l), \tag{3.22}$$

and similarly for τ^{**} and W^{**}. In the worst cases the relaxation factor ω was taken as low as 0.3, although no extensive optimization of this parameter was carried out. For these large hump sizes, around 50 iterations were required for the same degree of accuracy.

It may be noted that the results discussed in the following section have been

computed by the method discussed and by an alternative method as well. One of the authors (O. R. B.) has developed a spectral method in which the longitudinal flow and crossflow are uncoupled by use of the new variable

$$\sigma^{**} = \tau^{**} - \frac{k}{l} W_Y^{**}.$$

Then, in place of (3.19), there results a similar matrix equation for σ^{**} alone, together with a corresponding one for W_Y^{**} alone. The pressure is determined by σ^{**} (and the surface shape), independently of W_Y^{**}. The remaining details of the method are as described above, including the solution procedure. Results were calculated on a uniform Y-grid, using Richardson extrapolation for improved accuracy. The coordinate scaling (3.6) was found to produce results of the same accuracy, without Richardson extrapolation, with far fewer gridpoints in the Y-direction.

4. Discussion of results

The solution procedure just outlined is based on neglecting the nonlinear terms in the first iteration. Consequently, the computation in the spectral plane (k, l) can be checked against analytical formulas for the linearized solution in spectral variables. Comparisons of this type were made for a variety of cases with excellent agreement. In addition, the results in the physical plane (X, Z) via the discrete fast Fourier transform compared well with independent numerical integrations from linearized theory, which were carried out to much greater precision.

A periodic ridge

The only results available for checking the nonlinear computation are those of Sykes (1980), based on finite-difference solutions of the three-dimensional triple-deck equations for the periodic surface-height distribution

$$F(X, Z) = \begin{cases} \cos^2 \pi X \cos \dfrac{\pi Z}{L} & (|X| < 0.5, \text{ all } Z), \\ 0 & (|X| > 0.5, \text{ all } Z). \end{cases} \tag{4.1}$$

This configuration can be viewed as a range of hills and hollows aligned along the Z-axis. Sykes' application was to a stably stratified atmospheric boundary-layer flow, so that the usual pressure-interaction condition (3.10) was replaced by a zero-displacement condition for the upper-level air flow. (This problem also corresponds to Smith's (1976) pipe-flow equations.) In order to stabilize his marching computation, Sykes used a pseudospectral computation in the Z-direction; i.e. he evaluated Z-derivatives from a Fourier-series representation of the velocity components, truncating the Fourier series after the third harmonic. Higher harmonics were found to grow too rapidly to be retained. For purposes of comparison, our spectral program was modified to use the same zero-displacement condition, and the same spectral grid in the Z-wavenumber variable (i.e. the same number of terms in the Z-Fourier series). It may be noted that there is no difficulty in utilizing more Z-wavenumber gridpoints in the spectral method, since the marching instability does not occur in the spectral method.

Figure 2 (*a*) compares results of the spectral program with those of Sykes for the longitudinal surface stress on the lines of symmetry through the hump, $Z = 0$, and the hollow, $Z = L = 0.8$. (Sykes' data are taken from the dotted curves in his

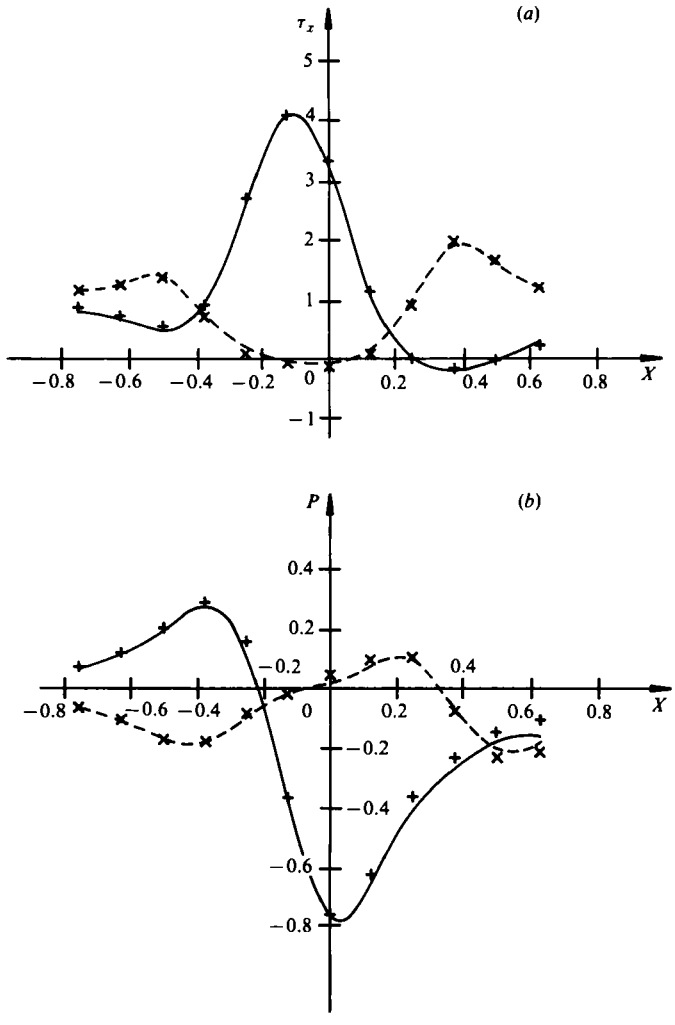

FIGURE 2. Distribution of properties on periodic ridge for $h = 2$: ——, Sykes' results, $Z = 0$; – – – –, Sykes' results, $Z = L = 0.8$; (+, ×), present results for $Z = 0$ and 0.8. Spectral results h^2 extrapolated with $J = 21$ and 41. (*a*) Longitudinal shear stress. (*b*) Pressure (spectral results shifted by 0.05; see text).

figure 8.) The height of the hump (and depth of the hollow), $h = 2$, is large enough to produce separated regions behind the humps and in the hollows. The spectral grid is coarser but more extensive than Sykes' grid, corresponding to the physical range $-4 < X < 4$; Sykes' computational grid covered the range $-0.8 < X < 0.6$ (approximately), with the flow represented by formulas from linearized theory for $X < -0.8$. Nevertheless, the two computations compare quite well, with the proviso that both are based on only eight terms (plus constant) in the complex Fourier series for the Z-variation. Additional spectral computations were made with double the number of Z-harmonics; the results were within about two percent of those of figure 2(*a*), suggesting that Sykes' cosine-shaped configuration has only a small degree of nonlinear interaction in the Z-direction, at least for $h = 2$.

The pressure distributions are shown in figure 2(*b*). Originally the spectral results

Grid	K	$k_{\max}$	L	$l_{\max}$	J	η_∞
1	64	7.111	64	5.079	11	0.95
2	32	7.226	32	5.161	11	0.95
3	32	10.323	32	10.323	11	0.95
4	32	10.323	32	10.323	21	0.95

TABLE 1. Grid parameters

lay about 0.05 above the results of Sykes (the range of P is from about -0.7–$+0.3$). However, after shifting the spectral data down by this amount (as plotted), the two sets of data agree about as well as those for the surface stress. The cause of this bias error can be explained as follows. The absolute pressure level is determined by the boundary condition that pressure approach the free-stream value (zero) at infinity. This condition is represented spectrally by requiring the integral transform of the pressure to vanish at the origin $k = l = 0$. However, the finite transform interprets this condition as vanishing of the mean of its periodic physical pressure. For an axisymmetric protuberance this bias error diminishes as the reciprocal of the area of the double period of the transform $(1/X_{\max} Z_{\max})$, and so the error is negligible for typical grids. In the case treated by Sykes the bias error diminishes only as the reciprocal of the X-period, since the flow actually is periodic in the Z-direction. Consequently, the bias error is more significant for that case. Sykes established his pressure level by matching to the linear theory, and that approach would improve the spectral results also for this case of transversely periodic topography.

Isolated peaks and hollows

For ease of reference the various combinations of grid parameters used for the following numerical studies are given in table 1. In the computational cycle the N gridpoints of the physical and spectral coordinates are connected by the relation

$$\Delta k \, \Delta X = 2\pi/N,$$

and similarly for ΔZ and Δl. This relation arises from the replacement of the integral transform by the finite transform, corresponding to the maximum wavenumber allowed in the spectral solution. In the table J denotes the number of Y-gridpoints, K the number of k-gridpoints (and similarly L for the l-grid), while $k_{\max}$ and $l_{\max}$ denote the half-range of the spectral coordinates: $-k_{\max} \leqslant k < k_{\max} - \Delta k$, $-l_{\max} \leqslant l < l_{\max} - \Delta l$. The asymmetry of the k- and l-ranges is only apparent; the periodicity of the discretized solution requires that, in particular, $P^{**}(k_{\max}, l) = P^{**}(-k_{\max}, l)$, and similarly for $l_{\max}$.

The second class of topography chosen for this study is the finite cosine-squared hump shown in figure 1:

$$F(X, Z) = \begin{cases} \cos^2 \tfrac{1}{2}\pi R & (R < 1), \\ 0 & (R > 1), \end{cases} \tag{4.2}$$

where $R^2 = X^2 + Z^2$. The linearized solution for this case was considered in detail by Smith *et al.* (1977), providing a basis for evaluation of nonlinear effects. Following Sneddon (1979), the double Fourier transform of (4.2) can be written in the form

$$F^{**}(k, l) = 2\pi \int_0^1 r J_0(\lambda r) \cos^2 \tfrac{1}{2}\pi r \, \mathrm{d}r, \tag{4.3}$$

where $\lambda^2 = k^2 + l^2$. Equation (4.3) was used to generate the surface height transform for the solutions given here. The alternative direct transformation of (4.2) using the FFT was carried out also with no appreciable difference in the results. Since this transform needs to be evaluated only once, there was no appreciable difference in computing time either.

The cosine-squared hump of (4.2) has a restricted range in physical space, being identically zero outside a unit radius. On the other hand, in transform space it has infinite range, decaying only algebraically to zero with increasing radius. A third class of surface topography with the opposite character is represented by the shape

$$F(X, Z) = [(1 + X^2)(1 + Z^2)]^{-1} \tag{4.4}$$

for all X and Z. This function has the Fourier transform

$$F^{**}(k, l) = \pi^2 \exp(-|k| - |l|). \tag{4.5}$$

Thus (4.4) displays a slowly decaying height in physical space, while (4.5) shows a very rapid decay in transform space. Height contours of the shape (4.4) are displayed in figure 3; the shape appears to be that of a rounded pyramid over most of its elevation. In the following discussion we shall refer to shapes (4.2) and (4.4) as cosine-squared shapes and pyramid shapes respectively.

Surface properties for the cosine-squared hump with $h = \pm 3$ are shown in figure 4. The computations were based on spectral grid 3, listed in table 1. Grid 4 was utilized also to test the effect of refining the Y-grid size; the results for the two grids differed by at most 2%. The pressure distribution along the centreline ($Z = 0$) is presented in figure 4(*a*). The linearized solution is shown as well, and is scaled to $h = 3$ for ease of comparison. For the hump the general features are seen to be the same for both linear and nonlinear results, although the pressure extremes are larger for the nonlinear results. On the other hand, the pressure distribution for hollow ($h = -3$) is quite different from the linear theory, with much smaller suction occurring. The pressure peak at reattachment rises to the same level as for the hump, however. An inflection in the pressure over the deepest part of the hollow is evident in the figure, suggesting that a pressure plateau is starting to develop like those observed in the two-dimensional solution of Burggraf & Duck (1981) and of Rizzetta *et al.* (1978).

The corresponding surface values of the shear stress in the mainstream direction are shown in figure 4(*b*), with similar conclusions as for the pressure. In this case, the negative stress over the bottom of the hollow indicates a sizable separated region there, as would be expected with incipient development of a pressure plateau. The separated region for the hump is much smaller than for the hollow. A pronounced overshoot in the shear is observed downstream near the end of the hollow, with corresponding undershoot of the pressure in figure 4(*a*). The crossflow surface shear stress is shown in figure 4(*c*) for the line $Z = -0.5$ parallel to the longitudinal centreline. Again the nonlinear and linearized solutions are similar over the entire hump, while the hollow shows an inflection in the crossflow shear followed by a strong negative peak halfway up the rear side of the hollow. Comparison with figure 4(*b*) shows that this peak in the crossflow shear occurs just downstream of reattachment.

Figures 5(*a–c*) show contours of pressure and of longitudinal and crossflow shear components for the cosine-squared hump. The top part of each figure is for the hump with $h = +3$, while the lower part is for $h = -3$. Since the linearized solution is symmetric in Z this form of presentation allows easy assessment of nonlinear effects. At large distances the contour patterns for the hump and the hollow are similar; however, near the hump (and hollow) the larger amplitude of the disturbance results

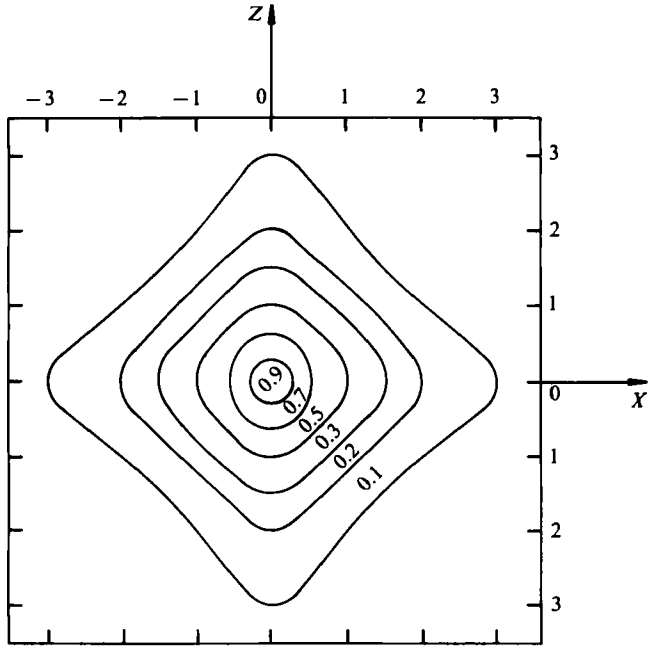

FIGURE 3. Height contours for the quasipyramidal shape of (4.4).

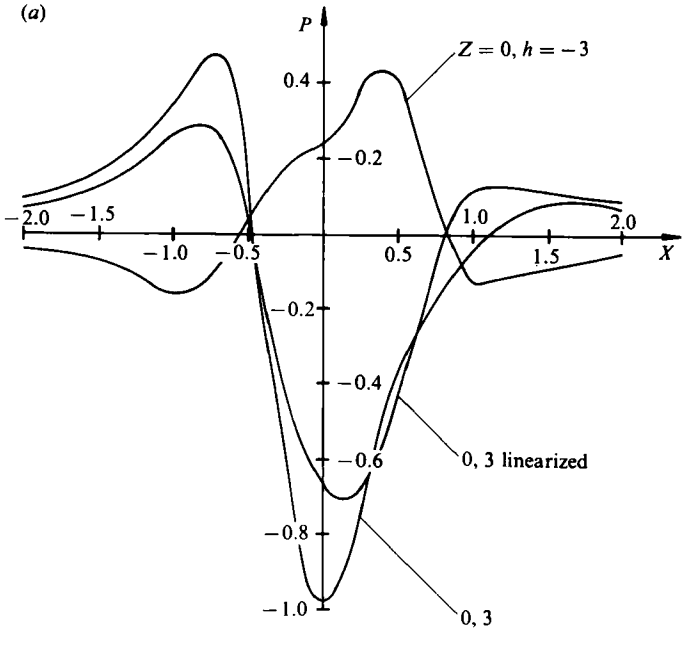

FIGURE 4(*a*). For caption see facing page.

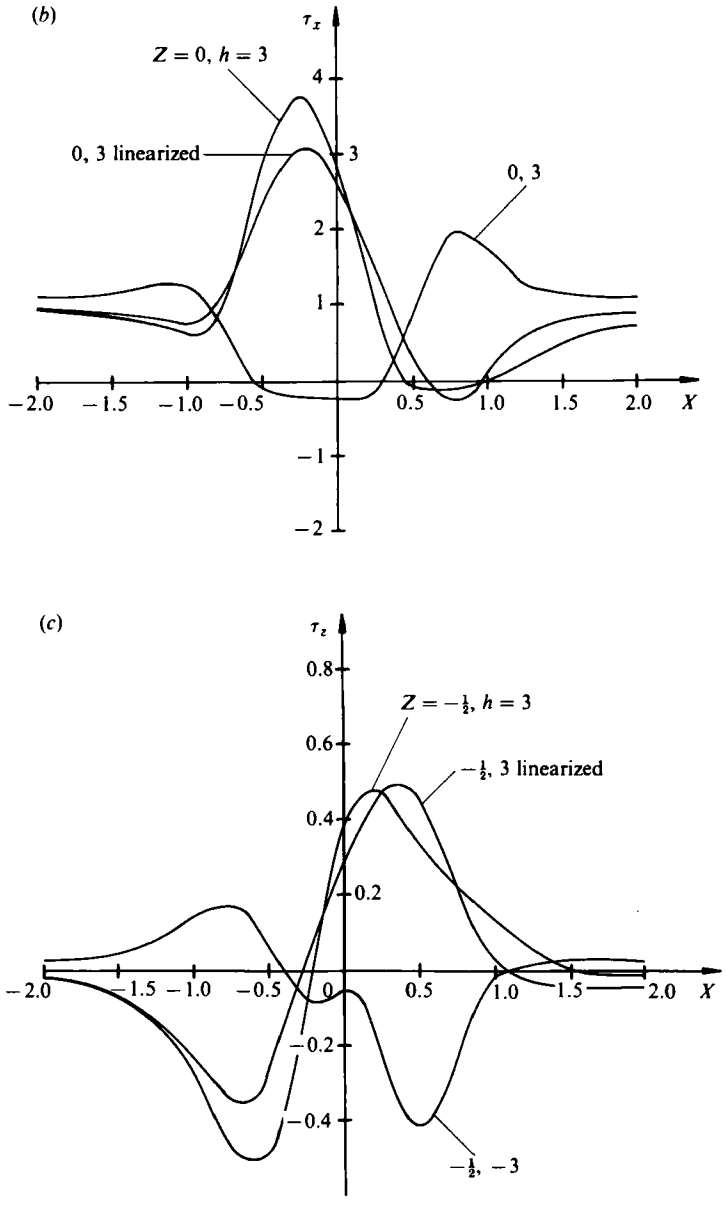

FIGURE 4. Distribution of properties on cosine-squared shape, $h = \pm 3$. (*a*) Pressure. (*b*) Streamwise wall shear. (*c*) Crossflow wall shear.

in a distortion of the contours from their linearized counterparts. This effect is most evident in the separated region at the bottom of the hollow, especially for the surface shear in figures 5(*b*, *c*). The corridor effect noted in the linearized solutions of Smith *et al.* (1977) is evident in the appearance downstream ($X > 2$) of the off-axis contours $\tau_x = 1$ in figure 5(*b*).

The singular points at separation and reattachment are of special interest; these occur at the intersections of the zero contours of the longitudinal and crossflow surface shear. There are only two such singularities for the cosine-squared shape, both on

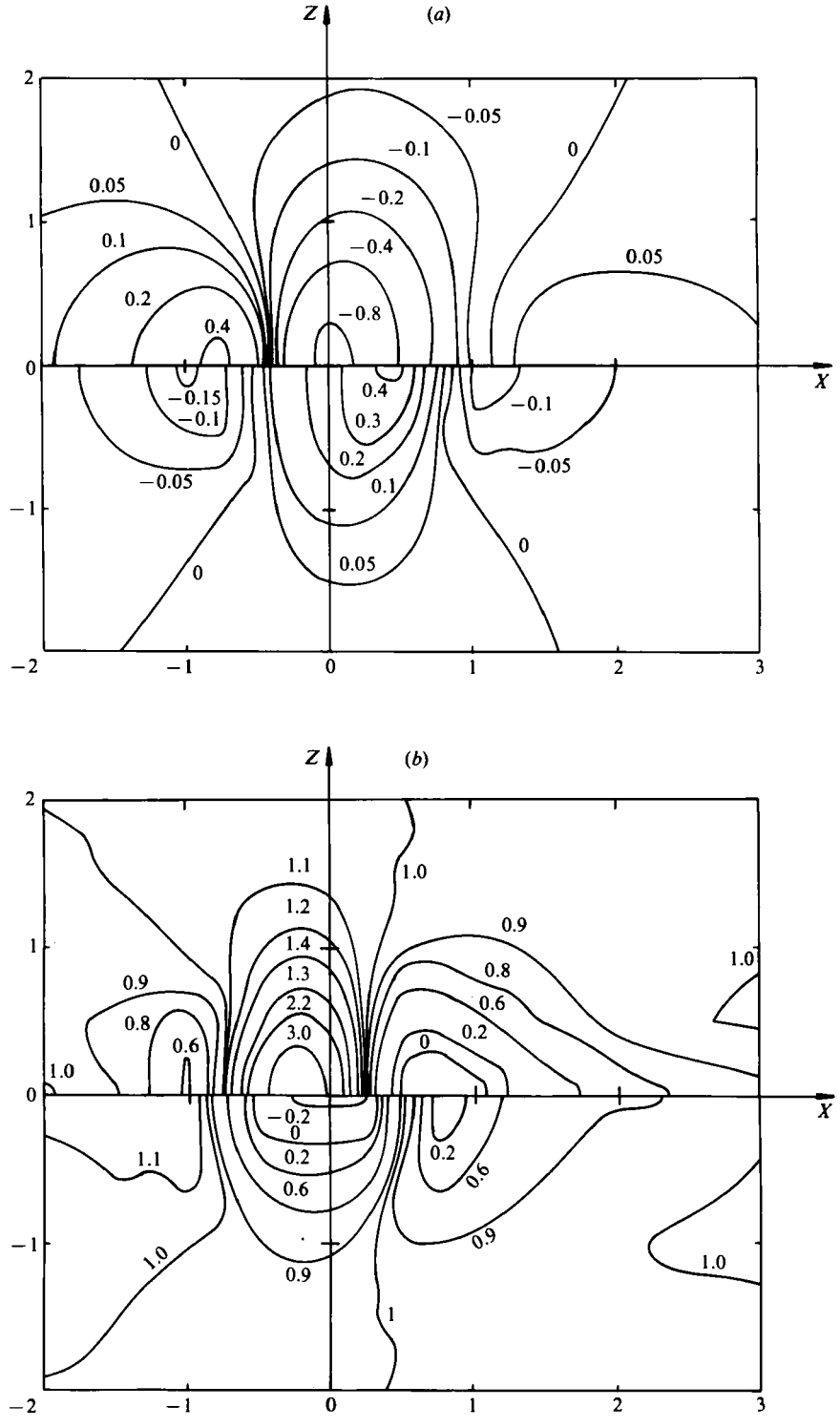

FIGURE 5(*a*,*b*). For caption see facing page.

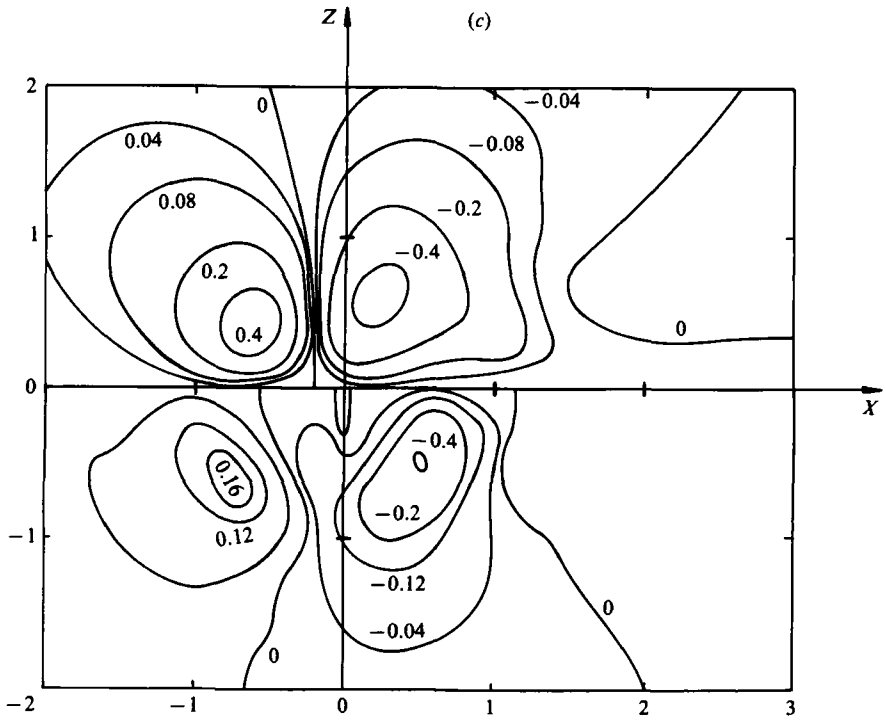

FIGURE 5. Contours for cosine-squared shape: upper, $h = +3$; lower, $h = -3$. (*a*) Pressure. (*b*) Streamwise wall shear. (*c*) Crossflow wall shear.

the centreline $Z = 0$. Those for the hump both occur on its downstream side. The signs of the surface shear components in the neighbourhood of the singularity determine its type: the singularity at $X = 0.5$ is a separation node, while that at $X = 1.12$ is an attachment saddle point. For the hollow the singularity at $X = -0.53$ is a separation saddle point, while that at $X = 0.32$ is an attachment node, a reversal of the situation for the hump. These results agree with the surface 'streamline' patterns obtained by Sykes (1980) for the case of an infinite row of humps and hollows. Lighthill (1963) and others have shown that the number of nodal points must exceed the number of saddle points exactly by two for a finite closed body. Since our case can be regarded as a local perturbation on such a body, any additional nodes and saddles must exactly cancel in number. The count of singularities above is seen to satisfy this condition.

Numerical solutions for the cosine-squared hump were attempted for the case $h = 5$ also, based on spectral grid 3. The results were qualitatively the same as described above; however, the separated region was slightly more extensive, resulting in spurious oscillations of the shear values in the separated region. Since no new features of the flow were evident, this computation was not refined. We shall consider instead the effects of modifying the shape of the protuberance.

For the rounded pyramid of (4.4) triple-deck solutions were computed for h in the range $-7.5 \leqslant h \leqslant 7.5$ for various choices of grid parameters. Results are shown only for the extreme cases: the hump with $h = 7.5$ and the hollow with $h = -7.5$. The centreline pressure and surface shears are shown in figure 6, again compared with the scaled-up results of linear theory. The comparisons are quite similar to those for the cosine-squared shape; the greater levels reached in figure 6 correspond to the greater

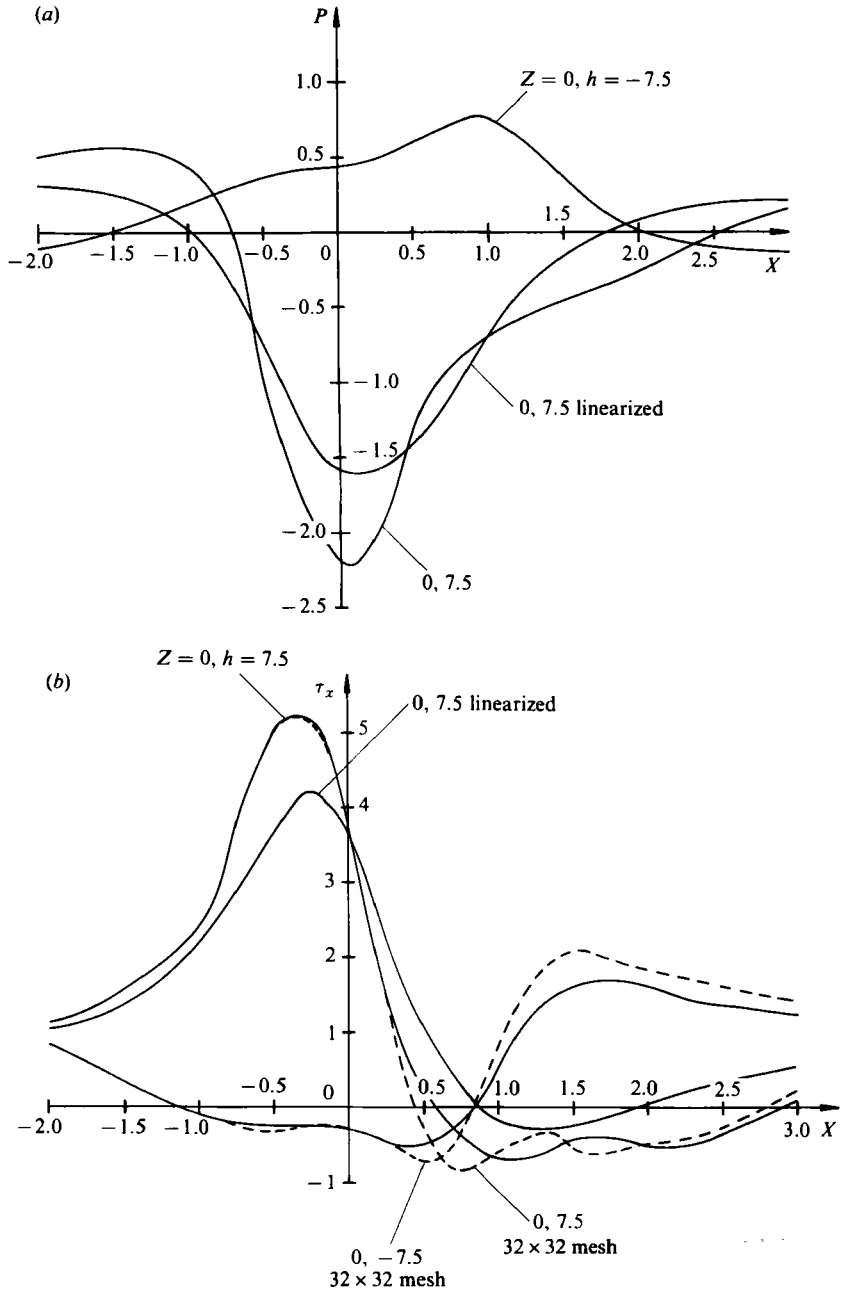

FIGURE 6(*a*,*b*). For caption see facing page.

amplitude of the surface height, while the greater range of the disturbance corresponds to the slower decay of height with distance for the 'pyramid' shape. The effect of grid size is illustrated in figure 6(*b*), where the dashed curves are for a 32 × 32 spectral grid, while the solid curves are for a 64 × 64 spectral grid. Both sets of solutions show an oscillation in the longitudinal shear in the reversed-flow region, but the amplitude is much reduced by use of the finer grid. All the results discussed below are for the 64 × 64 grid.

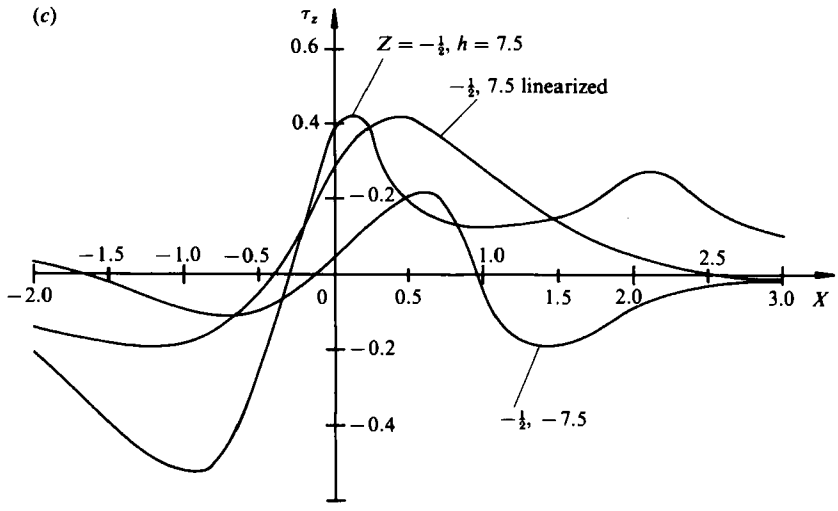

FIGURE 6. Distribution of properties for pyramidal shape, $h = \pm 7.5$: ——, grid 1; – – – –, grid 2. (*a*) Pressure. (*b*) Streamwise wall shear. (*c*) Crossflow wall shear.

Contours of pressure and longitudinal and crossflow shear at the surface are shown in figure 7 for the pyramid shape, again with the upper half-figure for the hump ($h = +7.5$) and the lower half-figure for the hollow ($h = -7.5$). The pressure levels are seen to be roughly double those in figure 5 (*a*), and the rate of decay is much slower, corresponding to the greater amplitude and range of the surface topography in this case. The longitudinal surface stress contours show these features as well. As remarked before, the reversed-flow region covers much of the bottom of the hollow. Note also that the contours on the forward part of the 'pyramid' topography tend to follow the height contours, especially in the hollow. The far-field pattern in this case cannot be seen on the scale of the figure, but the numerical results do not show the same behaviour as those for the cosine-squared configuration. In particular, there is no sign of the 'corridor effect' of Smith *et al.* (1977). This difference in the far-field behaviour may be attributed to the fact that for the pyramid the height decays so slowly that the shape controls the local flow properties all the way to infinity, whereas the bounded range of the cosine-squared shape makes it appear as an isolated delta-function on a flat surface from the far-field point of view.

Comparison of figures 5 (*b*) and 7 (*b*) shows that the reversed-flow regions for the 'pyramid' are more extensive than those for the cosine-squared hump, corresponding to the greater range and amplitude of the former. In the former case the separation point lies quite near the tip of the hump, whereas that for the cosine-squared hump lies about halfway down its back. Thus the local flow conditions for separation are quite different in these two cases, and the resulting types of separation and reattachment may be expected to differ as well.

Figures 8 (*a*, *b*) show the surface 'streamlines' for the pyramidal hump and hollow respectively. These curves are the paths taken by particles located an infinitesimal distance above the surface, and are determined by the equation

$$\frac{\mathrm{d}Z}{\mathrm{d}X} = \frac{\tau_z}{\tau_x},$$

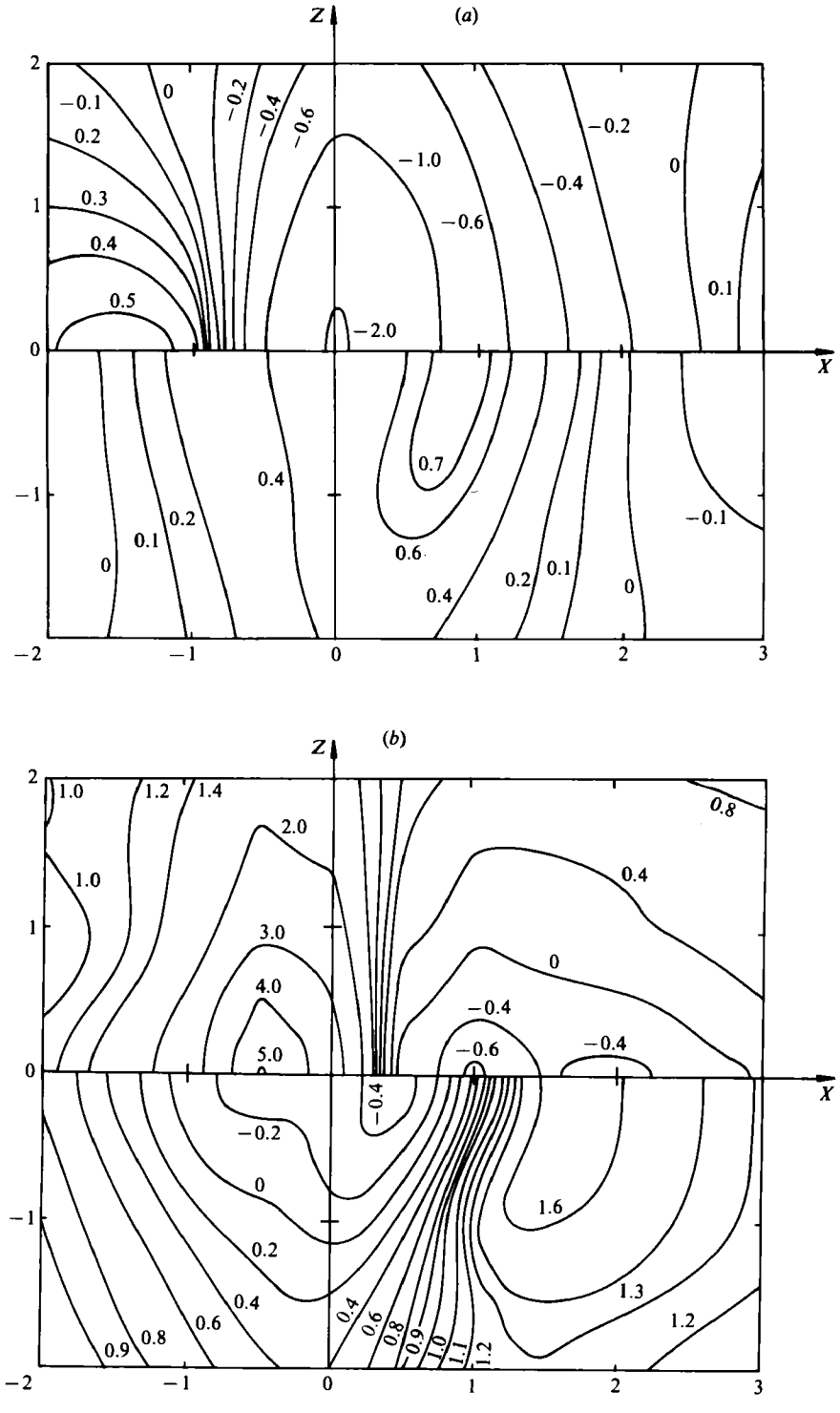

FIGURE 7(*a*, *b*). For caption see facing page.

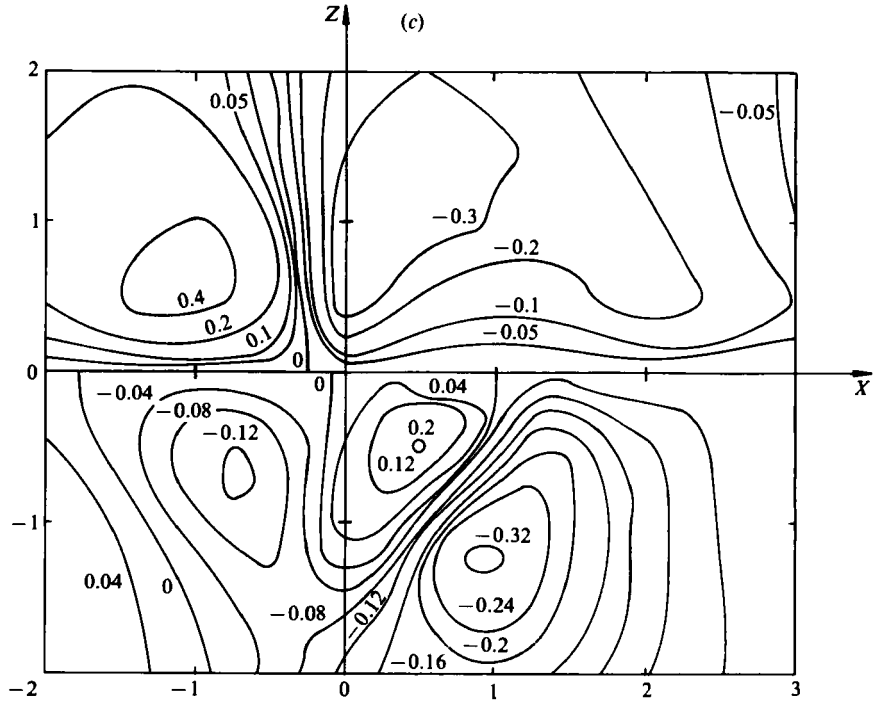

FIGURE 7. Contours for the pyramidal shape: upper, $h = +7.5$; lower, $h = -7.5$. (*a*) Pressure. (*b*) Streamwise wall shear. (*c*) Crossflow wall shear.

where τ_x and τ_z are the longitudinal and crossflow shear shown in figures 7 (*b*, *c*). The solution curves were determined by Runge–Kutta integration, with τ_x and τ_z determined locally by four-point linear interpolation using the four corner points of the original data grid. Most particle-path integrations were originated at points evenly spaced along the left edge of the plots. However, to fill out the field, it was necessary to originate some paths on the right edge, integrating backwards along the trajectory; for the hollow (figure 7*b*) the enclosed central area required integrating both ways from origins on $X = 0$. Certain of these pathlines are shown as terminating artificially in the middle of the flow field; this was done for the purpose of clarity in interpreting the figures and should not be taken as being physically meaningful.

The zero-contours of longitudinal and crossflow surface shear intersect only on the longitudinal centreline for the pyramidal hump. The directions of the surface stress vectors at these two points in figure 7 (and the surface streamlines in figure 8*a*) show that the singularity at $X = 0.45$ is a nodal point of separation, while that at $X = 2.90$ is an attachment saddle point. These classifications are the same as for the cosine-squared hump. However, when the pyramidal hollow is considered (figures 7, 8*b*), the conclusions are different. The singularities on the centreline in this case are saddle points at both separation point ($X = -1.12$) and reattachment point ($X = +0.83$). The necessary cancelling nodes lie off-axis just ahead of the transverse line through the bottom of the hollow, at $X = -0.15$, $Z = \pm 1.09$. These nodes are spiral foci exhibiting weak convergence, indicating that they are points of separation. The stronger upstream saddle point of separation is seen to be consistent with the direction of the flow entering the hollow; the sharply skewed height contours of

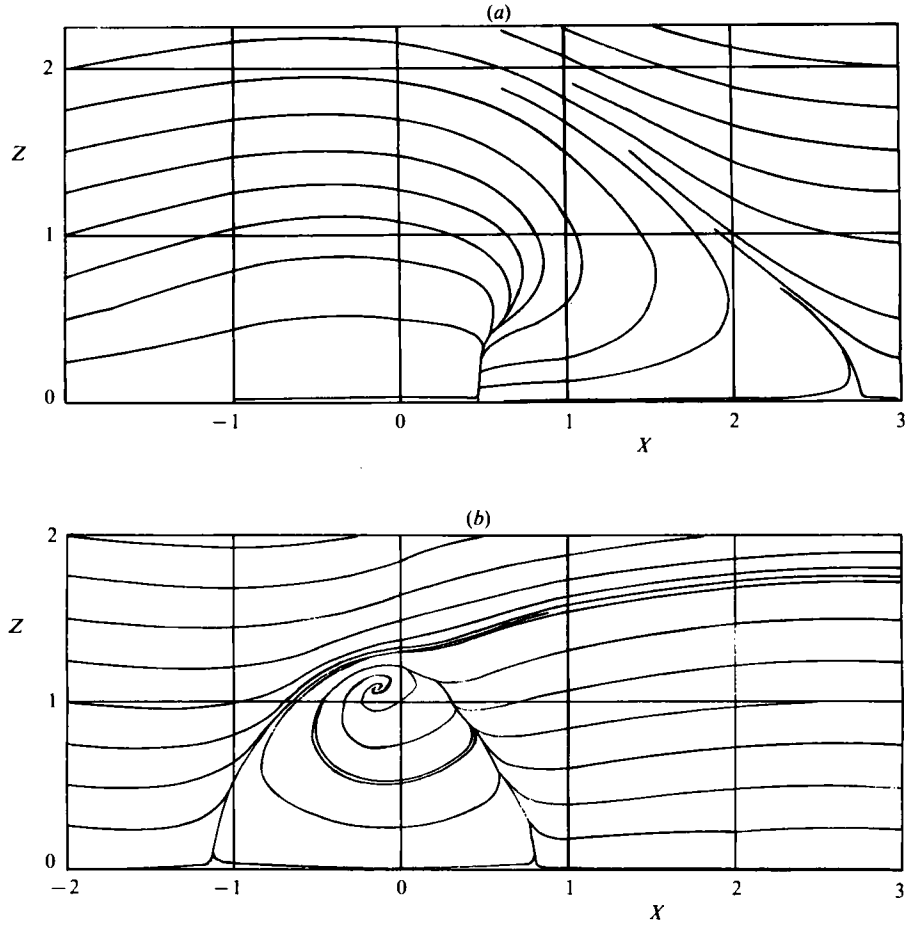

FIGURE 8. Surface streamlines for pyramidal shape. (*a*) Hump for $h = +7.5$. (*b*) Hollow for $h = -7.5$.

the pyramidal shape induce a crossflow pressure gradient that causes the upstream flow to converge toward the centreline. This convergence to the axis is seen from figure 7(*c*) to reverse at $X = -1.78$, after which a weak divergence occurs in anticipation of the approaching saddle point. The reattachment saddle corresponds to the channelling of the flow toward the axis by the strongly converging height contours as the flow climbs the rear surface of the hollow.

For the hump the streamlines near the line of symmetry ($Z = 0$) flow around the hump and then close in to the separation point partway down the leeward side of the hump. The streamlines farther out branch away from the attachment saddle point downstream. All points on the surface are accessible by surface flow from upstream. The case of the hollow contrasts sharply, with a large region of inaccessibility to surface streamlines coming from upstream. The streamline stemming from the point of separation is a limit line of separation that does not close back into a downstream reattachment point. Tracing the limit line of attachment away from the attachment point on the line of symmetry, it is seen that it evolves from a limit cycle, within which the streamlines diverging from the attachment line converge to a spiral focus, suggesting the origin of a separation vortex springing from the surface. The locations

of these vortical separation points (one on each side of the line of symmetry) are in the lateral corners of the pyramid, rather high up from the bottom. The more-rounded shape of the cosine-squared hollow does not produce such a phenomenon.

The saddle-to-saddle streamline connection in figure 8 (*b*) is not a stable configuration as a topological structure; that is, a slight lateral displacement of one saddle point relative to the other breaks the connection, so that some fluid particles near the singularities would follow paths far removed from those of the undisturbed configuration. In the case of figure 8 (*b*) such a disturbance would result in particles from one recirculatory cell passing across the central axis into the other cell. Physically this situation could correspond to an oscillatory motion of the separation point, and the flow pattern shown in the figure would then represent an average state. The question of the dynamic stability of such a perturbation could be answered only by analysis of the unsteady equations of motion.

In conclusion, the spectral method is confirmed to be an efficient technique for treating flows involving appreciable areas of flow reversal, bypassing many of the difficulties encountered in conventional finite-difference methods. For smooth surfaces the technique is especially efficient from the point of view of requiring surprisingly few gridpoints for reasonable accuracy; this feature of the method makes it a powerful technique for computing three-dimensional flows of this type. On the other hand, application of the method is limited by the usual restrictions of convergence of the Fourier transform, so that surface shapes with discontinuities of slope are more difficult to treat. As an example, the method has been applied by one of the authors (O.R.B.) to the flow past a hemispherical bump on a plane wall; in this case both the Fourier transform and the numerical solution converge, but an oscillation is evident in the wall-shear distribution. The results show that the amplitude of the oscillation decreases linearly with spectral grid size. However, it is estimated that about 64 megabytes of computer storage would be required to reduce the amplitude to under 1 %, contrasting sharply with the results described above, all of which ran in under one megabyte of storage.

This research was sponsored by the Office of Naval Research, United States Navy, under Contract N00014-76-C-0333, NR 061-194.

REFERENCES

BURGGRAF, O. R. 1976 The three-dimensional triple deck. In *Workshop on Viscous Interaction and Boundary-layer Separation, Ohio State University, 16–17 August 1976.*

BURGGRAF, O. R. & DUCK, P. W. 1981 Spectral computation of triple-deck flows. In *Numerical and Physical Aspects of Aerodynamic Flows* (ed. T. Cebeci). Springer.

COOLEY, J. W. & TUKEY, J. W. 1965 *Math. Comp.* **19**, 297.

DUCK, P. W. 1980 *Z. angew. Math. Phys.* **32**, 24.

JOBE, C. E. & BURGGRAF, O. R. 1974 *Proc. R. Soc. Lond.* A **340**, 91.

LIGHTHILL, M. J. 1963 Introduction. Boundary layer theory. In *Laminar Boundary Layers* (ed. L. Rosenhead), chap II. Oxford University Press.

MESSITER, A. F. 1970 *SIAM J. Appl. Maths* **18**, 241.

NEILAND, V. YA. 1969 *Izv. Akad. Nauk SSSR, Mekh. Zhidk. Gaza* **4**, 40.

RIZZETTA, D. P., BURGGRAF, O. R. & JENSON, R. 1978 *J. Fluid Mech.* **89**, 535.

SMITH, F. T. 1976 *Mathematika* **23**, 62.

SMITH, F. T. 1980 *J. Fluid Mech.* **99**, 185.

SMITH, F. T., SYKES, R. I. & BRIGHTON, P. W. M. 1977 *J. Fluid Mech.* **83**, 163.

SNEDDON, I. M. 1979 *Intl J. Engng Sci.* **17**, 185.
STEWARTSON, K. 1969 *Mathematika* **16**, 106.
STEWARTSON, K. 1974 *Adv. Appl. Mech.* **14**, 145.
STEWARTSON, K. 1981 *SIAM Rev.* **23**, 308.
STEWARTSON, K. & WILLIAMS, P. G. 1969 *Proc. R. Soc. Lond.* A **312**, 181.
SYKES, R. I. 1978 *Proc. R. Soc. Lond.* A **361**, 225.
SYKES, R. I. 1980 *Proc. R. Soc. Lond.* A **373**, 311.